coatings

MDPI

Article

The Microstructure and Mechanical and Corrosion Behaviors of Thermally Aged Z3CN20-09M Cast Stainless Steel for Primary Coolant Pipes of Nuclear Power Plants

Fei Xue [1], Fangjie Shi [1], Chuangju Zhang [2], Qiaoling Zheng [2], Dawei Yi [3], Xiuqing Li [4] and Yefei Li [2,*]

[1] Life Management Center, Suzhou Nuclear Power Research Institute, Suzhou 215004, China; xuefei@cgnpc.com.cn (F.X.); shifangjie@cgnpc.com.cn (F.S.)
[2] State Key Laboratory for Mechanical Behavior of Materials, Xi'an Jiaotong University, Xi'an 710049, China; zchuangju@163.com (C.Z.); zhengql@xjtu.edu.cn (Q.Z.)
[3] College of Materials Science and Engineering, Xi'an University of Science and Technology, Xi'an 710054, China; yidawei19820608@163.com
[4] National Joint Engineering Research Center for Abrasion Control and Molding of Metal Materials, Henan University of Science and Technology, Luoyang 471023, China; li_xq@sina.cn
* Correspondence: liyefei@xjtu.edu.cn; Tel.: +86-29-82668606

Abstract: The effects of thermal aging time at 400 °C on the microstructure and mechanical and corrosion behaviors of Z3CN20.09M cast stainless steel were investigated; and the corresponding thermal aging mechanism was studied. It was revealed that the changes in mechanical properties after thermal aging were mainly caused by the iron-rich phase (α) and the chromium-rich phase (α′) produced by the amplitude-modulation decomposition of ferrite. A similar trend of thermoelectric potential during thermal aging was determined in relation to the Charpy impact energy. However, the corrosion resistance of Z3CN20.09M cast stainless steel deteriorates as thermal aging time increases. When the thermal aging is longer than 3000 h, the precipitation of G phase has a great influence on the corrosion resistance. The interfacial matching relationship between G phase and the surrounding ferrite was established by selected area electron diffraction of HRTEM. The relationship is of cube-on-cube phase boundary type. The impact fracture mechanisms in relation to thermal aging time were also studied and compared.

Keywords: cast stainless steel; thermal aging; interfacial matching relationship; corrosion resistance

Citation: Xue, F.; Shi, F.; Zhang, C.; Zheng, Q.; Yi, D.; Li, X.; Li, Y. The Microstructure and Mechanical and Corrosion Behaviors of Thermally Aged Z3CN20-09M Cast Stainless Steel for Primary Coolant Pipes of Nuclear Power Plants. *Coatings* **2021**, *11*, 870. https://doi.org/10.3390/coatings11080870

Received: 24 June 2021
Accepted: 19 July 2021
Published: 21 July 2021

1. Introduction

In the past few decades, nuclear power, well known as the clean energy technology, has played an important role in industrial applications because of its low-carbon, high-efficiency nature [1–3]. The nuclear reactor is the core of any nuclear power plant, and among them are production reactors, research reactors and power reactors. The most commonly used power reactor is the pressurized water reactor, mainly because it is safe and reliable, low cost and technologically mature. It has become the main reactor type of nuclear power development in China [4–6]. The pressurized water reactor is mainly composed of a primary coolant system, a secondary coolant system and a circulating water system [7]. The primary coolant pipes are part of the first stage of nuclear safety, inside of which is high-temperature, high-pressure and radioactive reactor coolant. Therefore, their integrity (without failure) plays an important role in the safe and normal operation of a reactor [8–11].

Z3CN20.09M cast austenitic stainless steel (containing 12%–18% ferrite) has been widely used in the primary coolant pipes of in-service pressurized water reactors [12]. This kind of stainless steel undergoes thermal aging embrittlement during long-term service in reactors (~288–327 °C, ~16 MPa), resulting in deficient impact toughness and poor corrosion resistance [13–15]. The main problem is that the cast austenitic stainless

steel parts in the main coolant pipeline of the primary circuit are pressurized; thus, it is difficult to detect their mechanical properties directly [16–19]. Therefore, the prediction model and evaluation procedure of thermal aging embrittlement behavior are especially important for in-service inspections, safety assessments and life extension activities of nuclear power plants.

In the authors' past work [11], the early effects of thermal aging time (0–3000 h, 400 °C) on the mechanical properties of Z3CN20.09M cast austenitic stainless steel were investigated. As the aging time increased, both the crack initiation energy and the crack propagation energy decreased. The impact toughness of the inner walls of the pipes was far greater than that of the outer walls. The present work is dedicated to investigating the microstructural, mechanical and corrosion properties of Z3CN20.09M cast austenitic stainless steel over a far longer thermal aging time range (0–15,000 h, 400 °C). Our main aims were to estimate and compare not only the mechanical performance metrics, but also the corrosion behaviors of alloys after different amounts of thermal aging. We also tried to enhance the reliability of a non-destructive method for testing the thermoelectric potential of cast austenitic stainless steel.

2. Materials and Methods

Z3CN20.09M cast austenitic stainless steel (containing 12%–18% ferrite) was used in the present work with the chemical composition listed in Table 1. In order to obtain the Z3CN20.09M cast duplex stainless steel, the "designed" chemical composition should be determined before casting, and the final chemical composition of the sample will differ from the designed one, as shown in Table 1. This always happens with cast steel and iron. Next, the Z3CN20.09M cast austenitic stainless steel was obtained by heating at 1050 °C for 4 h and then quenching in water.

Table 1. Chemical composition of Z3CN20.09M cast stainless steel (wt.%).

Element	C	Cr	Ni	Si	Mn	S	P	N	Fe
Designed Composition	0.03	20.19	8.92	1.27	1.13	0.01	0.02	0.03	Bal.
Measured Composition	0.03	20.96	9.31	1.03	0.94	0.02	0.01	0.04	Bal.

The accelerated thermal aging method was carried out at 400 °C, and the actual aging speed was 4–5 times faster than in actual service (~288–327 °C) [20–22] in order to shorten the aging time. Z3CN20-09M cast stainless steel was aged, in total, 15,000 h, and at the holding times of 272, 544, 1000, 2000, 3000, 6000, 10,000 and 15,000 h, the samples were taken out and marked for subsequent microstructural analysis, and mechanical and corrosive property tests.

The microstructures of Z3CN20.09M cast stainless steel before and after thermal aging were studied via optical microscope (OM, Leica DMI500M, Wetzlar, Germany), field emission scanning electron microscope (FE-SEM, Zeiss sigma HD, Jena, Germany) and transmission electron microscope (TEM, JEM-2100, Tokyo, Japan). The crystal structure and lattice constants of G phase ($Ni_{16}Mn_6Si_7$) were studied via selective area electron diffraction technique combined with TEM. The hardness, impact toughness, thermoelectric potential and corrosion resistance of the materials were tested in order to reveal the thermal aging mechanism. The specimens were as shown as Figure 1. The impact toughness tests were carried out on an impact testing machine, and the impact work of each specimen was measured at room temperature (JB-W500C, Jinan, China). Figure 2 shows the thermoelectric potential (TEP) measurement system (Homemade, Suzhou, China), which can be used to assess the change in TEP. Both hot and cold contact points are made of copper; the temperature difference between the two contact points causes the thermoelectric phenomenon of current in the loop, and the corresponding electromotive force refers to the TEP [23–25].

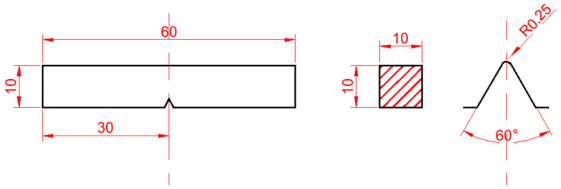

Figure 1. Dimensions of impact specimens (in mm).

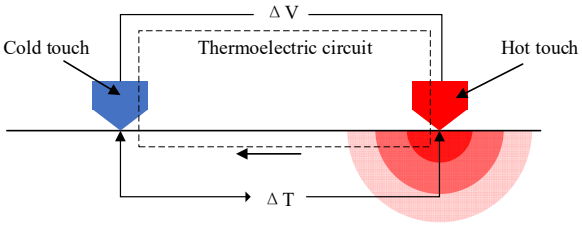

Figure 2. Thermoelectric test system.

The surface chemical states could be tested by X-ray photoelectron spectroscopy (XPS, AXIS ULtrabld, Manchester, England), since most of the detected signals came from the depth range of 1–10 atomic layers on the surface. In order to reveal the change in passivation film on the surface of Z3CN20-09M stainless steel during thermal aging, the XPS energy spectra of Fe, Cr, Ni and Mn were analyzed. The corrosion resistance of Z3CN20-09M cast stainless steel was evaluated via potentiodynamic polarization (Tafel) curve constructed through electrochemical experiments (CHI250, Shanghai, China). The reference electrode of the electrochemical test was a saturated mercurial electrode; the counter electrode was a Pt electrode; and a 3.5 wt.% NaCl solution was used for testing. The potential range of dynamic potential scanning was −0.6 to 0.3 V_{SCE} with a scanning rate of 1.67 mV/s.

3. Results and Discussion

3.1. Microstructure

The microstructures of Z3CN20-09M cast stainless steel after different amounts of aging are shown in Figure 3. The electron diffraction patterns of Z3CN20-09M cast stainless steel are shown in Figure 4. Based on Figures 3 and 4, double phases were determined which refer to a sharp-angle-type ferrite and austenite matrix. In this work, the morphology and distribution of ferrite did not change significantly with aging time. Chandra et al. [26] claimed that stress concentration occurs at the emerged sharp angles of ferrite after long-time thermal aging of cast stainless steel; this sharp-angle effect may deteriorate the mechanical properties of the steel. However, this work does not support that point of view, since the morphologies of ferrite phase in Z3CN20-09M cast stainless steel before and after thermal aging were more or less the same.

In order to quantitatively analyze the content and morphology changes of the ferrite phase over the course of thermal aging, the particle size distribution of ferrite (the maximum diameter of each grain in the crystal and its proportion) was calculated using the image analysis system of Leica OM. The results are shown in Figure 5. The transverse coordinate is the diameter of each ferrite grain, and the ordinate is the ratio of grains in the area to the total number of grains in this particle size range. Overall, there is not strong correlation among the volume fraction, the morphology of the ferrite phase and the duration thermal aging. The volume fraction of ferrite was about 13.0 before and after thermal aging. One could hardly observe any other phases with the OM.

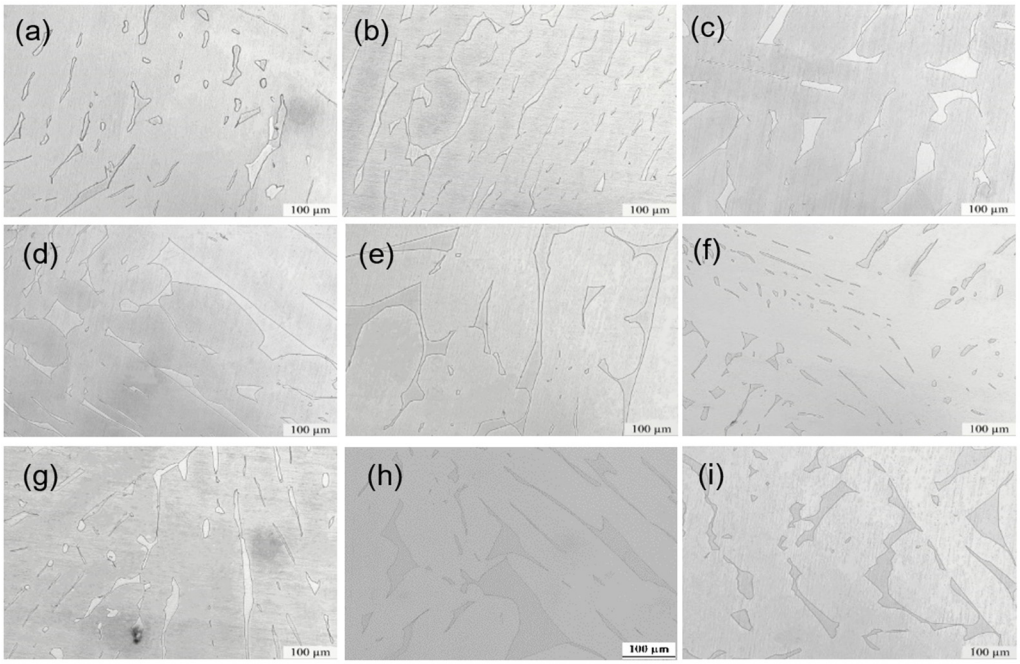

Figure 3. Microstructures of Z3CN20-09M cast stainless steel after different amounts of aging: (**a**) 0 h, (**b**) 272 h, (**c**) 544 h, (**d**) 1000 h, (**e**) 2000 h, (**f**) 3000 h, (**g**) 6000 h, (**h**) 10,000 h, (**i**) 15,000 h.

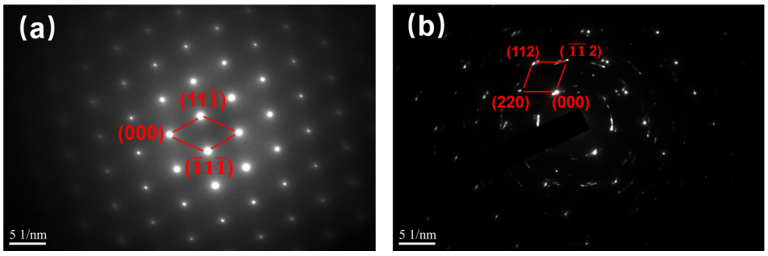

Figure 4. The electron diffraction pattern (TEM) of Z3CN20-09M cast stainless steel: (**a**) matrix; (**b**) sharp-angled grains.

Therefore, FE-SEM analysis was performed for specimens before and after thermal aging treatment, as shown in Figure 6. Generally, the thermal aging behavior of cast austenitic stainless steel is divided into two stages. The first stage corresponds to the thermal aging before 3000 h/400 °C. The iron-rich phase (α) and the chromium-rich phase (α′) are produced by ferrite amplitude-modulation decomposition. The second stage corresponds to the thermal aging after 3000 h/400 °C: the precipitated α′ phase aggregates and coarsens, and the obviously G phase precipitates occur. One can clearly observe from Figure 6 that the microstructure of ferrite phase was uniform before thermal aging, whereas after thermal aging for 15,000 h, there were significant mottled amplitude-modulation decomposition phases (α and α′) in which α′ phase was relatively coarse. The Cr-rich α′phase hinders the movement of dislocations, which greatly weakens the plasticity of the ferrite phase, thereby causing the material to undergo thermal aging and embrittlement. HRTEM images of the ferrite phase after thermal aging for 15,000 h are shown in Figure 7a,b. A large number of areas of dark G phase can be seen in the circles of the figure. The selected area electron diffraction pattern and corresponding FFT pattern along the [001] crystalline axis were detected, and they are shown in Figure 7b,c. After thermal aging at 15,000 h/400 °C, G phase and ferrite shared the same exponential crystal direction and plane [27–29]; i.e., G phase and ferrite have a cube-on-cube phase boundary relationship. The diffraction spots of the (044) crystal plane of G phase coincide with those of the (011) crystal plane of ferrite. Therefore, the lattice parameters ($a = b = c$ = ~1.12 nm) of G phase were approximately four times those of ferrite, which were all equal to 0.286 nm.

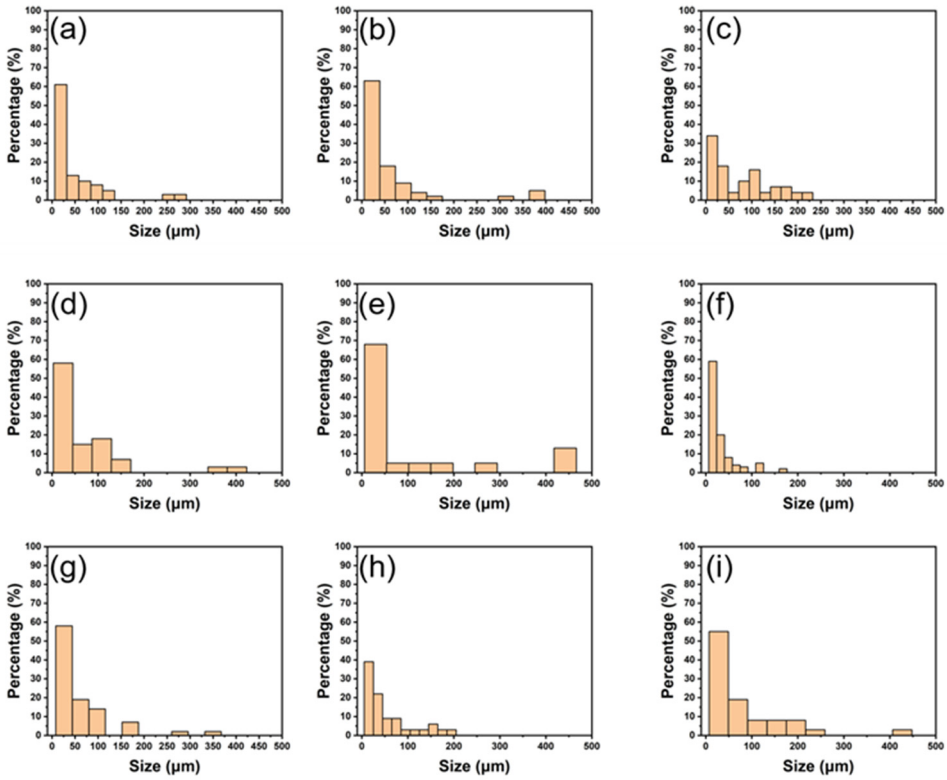

Figure 5. Particle size distribution of Z3CN20-09M stainless steel after different amounts of aging: (**a**) 0 h, (**b**) 272 h, (**c**) 544 h, (**d**) 1000 h, (**e**) 2000 h, (**f**) 3000 h, (**g**) 6000 h, (**h**) 10,000 h, (**i**) 15,000 h.

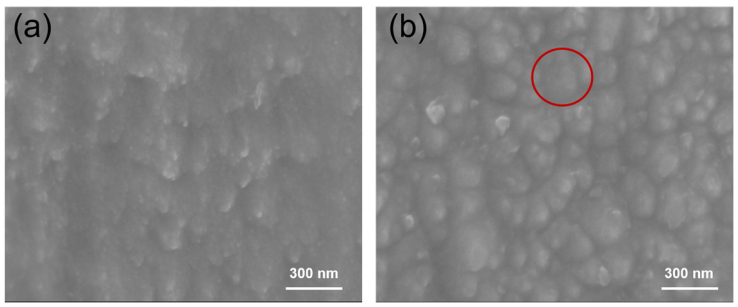

Figure 6. FE-SEM images of ferrite phase before and after thermal aging: (**a**) 0 h; (**b**) 15,000 h. The phase in the red circle is an α phase.

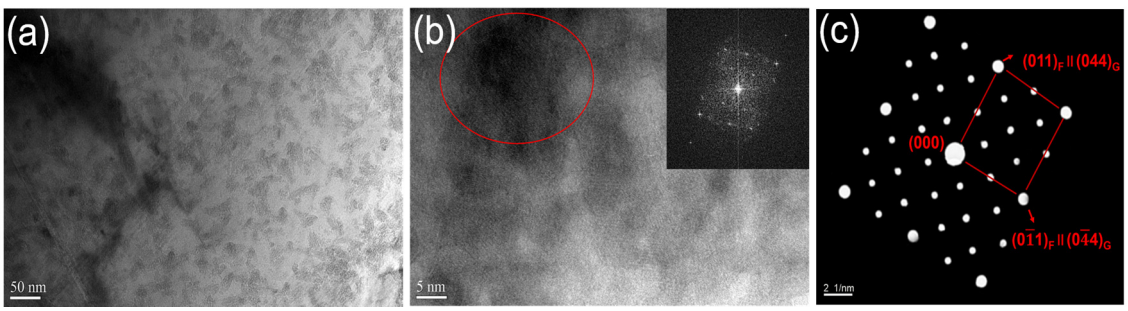

Figure 7. An HRTEM image of a ferrite phase (**a**); and an area electron diffraction pattern (**b**) and the corresponding FFT pattern (**c**) of Z3CN20-09M stainless steel after 15,000 h of aging. The red circles are G phase. The inset figure corresponds to the SEAD in (**b**).

3.2. Mechanical Properties

Figure 8a shows the variations of thermoelectric potential and impact energy with thermal aging time. The impact energy decreased rapidly with aging time until 3000 h. From 3000 to 15,000 h, the impact energy decreased very slowly; eventually it tended to be saturated. The saturated impact energy of Z3CN20-09M stainless steel is about 105 J. It is higher than the minimum safety shock absorption power (80 J) specified in the RCC-M standard [30]. It can be seen that domestic stainless steel has good impact toughness under long-term thermal aging. As for TEP of Z3CN20-09M stainless steel, it has an extremely similar trend for impart energy. In other words, the impact energy of the studied steel has a good linear relationship with TEP. The correlation coefficient of determination (COD) for the figure is ~0.96; therefore, the nondestructive testing equipment for TEP can be used in nuclear power plants. According to Figure 8b, one can obtain the impact work of Z3CN20-09M stainless steel simply by testing TEP values. However, we should note that for materials with long service lifetimes, the detection accuracy will be reduced: after thermal aging for 3000 h, when G phase began to emerge, the changes of TEP and impact work with aging were not obvious. As a result, the precipitation mechanism of G phase and its effects on the mechanical properties at the second stage of thermal aging are of great theoretical significance for nondestructive testing of thermal aging.

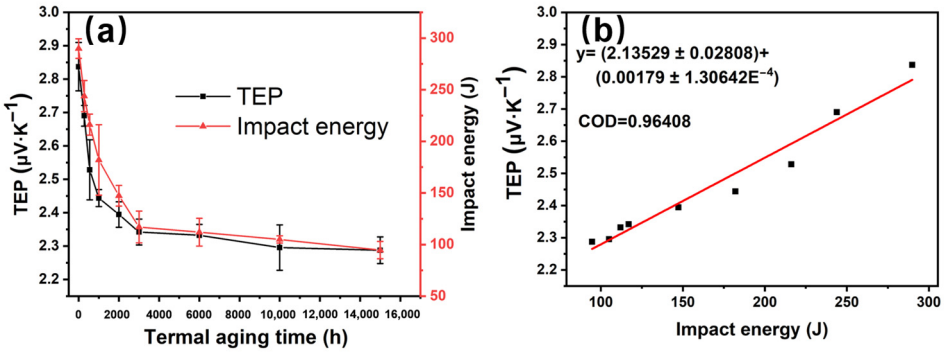

Figure 8. TEP and impact energy with respect to thermal aging time for Z3CN20-09M stainless steel (**a**), and the linear relationship between TEP and impact energy (**b**).

Figure 9 shows the FE-SEM images of impact fractures after different amounts of thermal aging. It can be seen that a large number of plastic deformations occurred at the impact fracture. As thermal aging time increased, the dimple gradually became shallower, and the number of dimples decreased gradually, indicating that the impact toughness also decreased. After 3000 and 15,000 h, the "fluvial-type" micro-fracture pattern could be observed, and some brittle cleavage fractures may have occurred (Figure 9b,c). Before thermal aging, the fracture mechanism of Z3CN20-09M cast stainless steel mainly showed microporous-agglomeration-based ductile fracturing. After considerable thermal aging, the fracture mechanism changed to a combination of brittle cleavage fracturing and microporous-agglomeration-based ductile fracturing.

Both the ferrite phase and the austenite phase in the initial material had good deformability and good ductility. During the thermal aging process, the ferrite phase underwent amplitude-modulation decomposition, resulting in a gradual decrease in the deformability of the ferrite phase and a gradual decrease in the toughness of the material. Therefore, cracks were first formed in the ferrite phase, and then the main cracks propagated along the fractured ferrite, and after reaching the austenite, the material fractured.

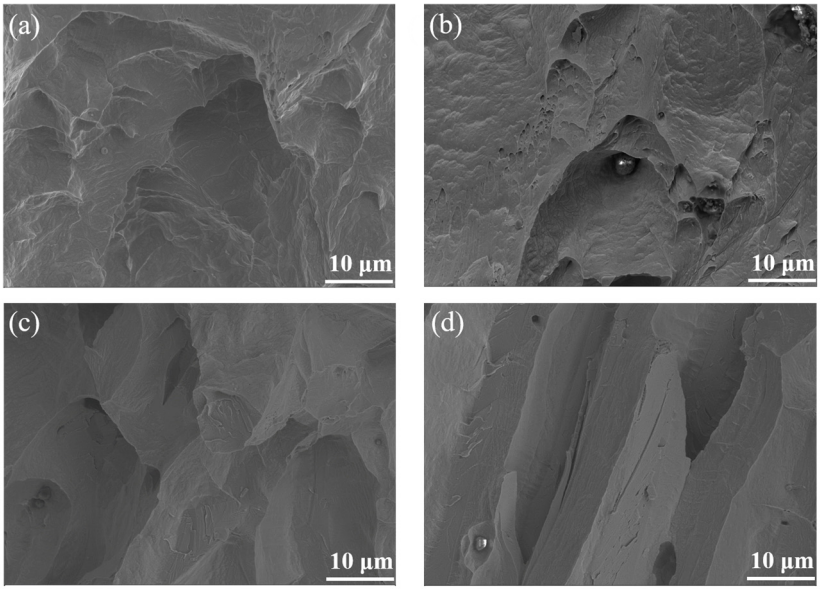

Figure 9. SEM images of impact fractures of Z3CN20-09M stainless steel after different lengths of aging time: (**a**) 0 h, (**b**) 544 h, (**c**) 3000 h, (**d**) 15,000 h.

The conventional Vicker's microhardness test is not suitable for the present alloys, since the grain size of ferrite is too small to be precisely measured; i.e., the austenite/ferrite phase boundary may affect the measurement results. Hence, the hardness of Z3CN20-09M cast stainless steel was further determined and analyzed by the nano-indentation method. Figure 10 shows the load–displacement curves of ferrite and austenite phases after thermal aging. It can be seen that as thermal aging time increases, the slopes of load–displacement curves of austenitic do not change obviously for the whole thermal aging duration. However, the slopes of load–displacement curves of ferrite increase significantly before 3000 h (Figure 10b), but there is not a notable change after 3000 h. Therefore, the thermal aging effect on microhardness was probably mainly restricted to the first 3000 h. Figure 10c gives the results of the microhardness values of Z3CN20-09M stainless steel after different amounts of thermal aging. Before thermal aging treatment, the hardnesses of ferrite and austenite were similar. As thermal aging time increased, the hardness of ferrite increased rapidly. As a result, the overall hardness of Z3CN20-09M stainless steel after thermal aging was mainly caused by the embrittlement of ferrite. In other words, due to the generation of the Cr-rich α'phase, the Cr clusters in the ferrite will prevent the movement of dislocations, resulting in dislocation plugging and pinning effects.

The ferrite phase's hardening tendency is just the opposite of the impact energy's trend, which is mainly related to the amplitude-modulation decomposition. In the process of amplitude-modulation decomposition, as thermal aging time increases, the degree of fluctuation of alloy composition increases, the hardness increases and the plastic deformability decreases.

The impact energy and the hardness change mechanism of the ferrite phase are correlated. The main reason is that the decrease in impact absorption energy and the increase in the hardness of the ferrite phase are both caused by the amplitude-modulation decomposition of the ferrite phase. The precipitation of the G phase also has related effects. The impact fracture process includes the initiation and propagation of cracks. In the process of crack propagation, they pass through both the ferrite region and the austenite region. Therefore, there is a risk in using the hardness of ferrite as a key index with which to evaluate thermal aging performance.

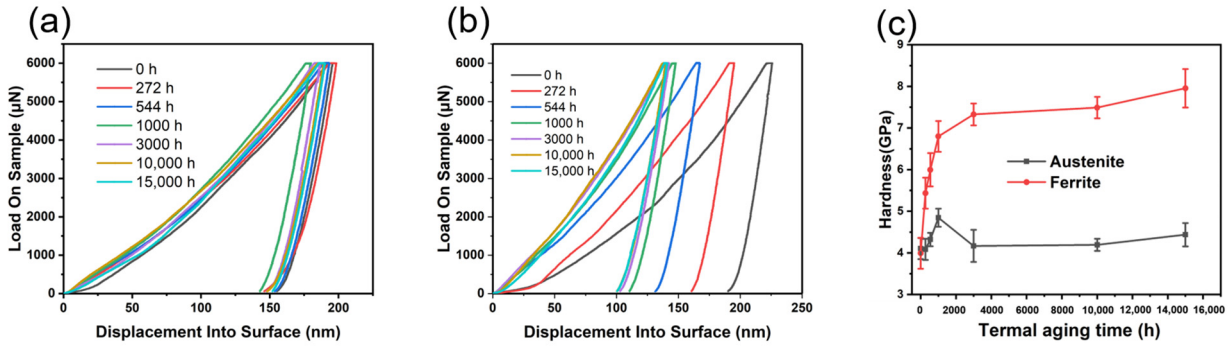

Figure 10. Load–displacement curves for the austenite (**a**) and ferrite (**b**) of Z3CN20-09M stainless steel after different amounts of aging. The computed microhardness is also given (**c**).

3.3. Corrosion Properties

Figure 11 provides the XPS energy spectra of chromium for Z3CN20-09M cast stainless steel after different amounts of aging (without immersion corrosion tests). The content of hexavalent Cr increased gradually with the thermal aging time, and the trivalent Cr continually decreased. Therefore, the dense Cr_2O_3 passivation film on the surface of stainless steel is gradually destroyed. Figure S1 gives the XPS energy spectra of iron. The content of non-valent iron decreased as thermal aging increased. Meanwhile, the contents of divalent and trivalent iron increased gradually, indicating that the iron on the surface of stainless steel was gradually oxidized during thermal aging. Therefore, as the thermal aging treatment continued, the stability of the surface-passivated film of Z3CN20-09M stainless steel became weak, and the corresponding corrosion resistance gradually reduced. For the energy spectrum of manganese, no peaks were detected before the thermal aging time of 544 h; after this critical time, the content of Mn increased. This phenomenon is closely related to the clusters of Mn in ferrite during the formation of G phase. Takeuchi et al. [31] confirmed that there exists a cluster of Mn inside the ferrite phase after much thermal aging of cast stainless steel by using 3D atomic probe technology (3DAP).

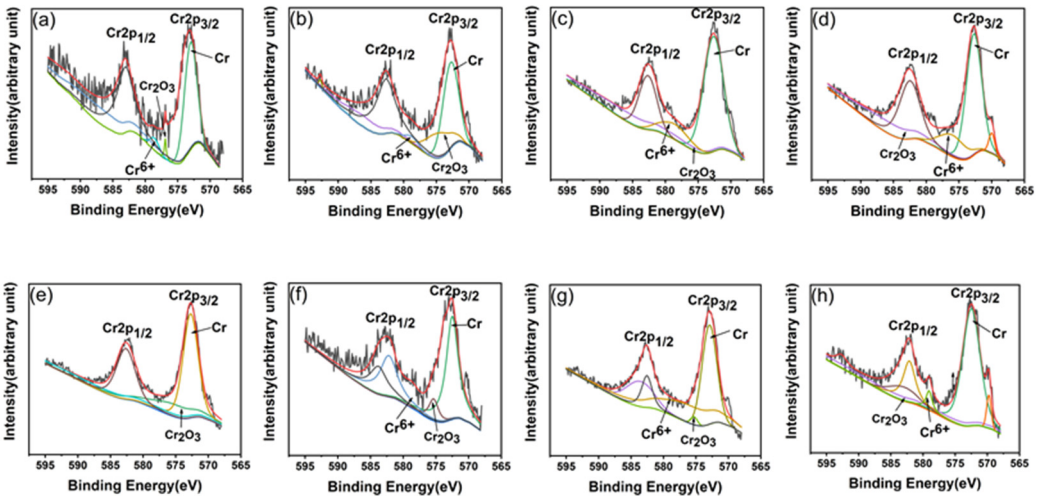

Figure 11. XPS energy spectra of chromium of Z3CN20-09M stainless steel after different amounts of aging: (**a**) 0 h, (**b**) 272 h, (**c**) 544 h, (**d**) 1000 h, (**e**) 3000 h, (**f**) 6000 h, (**g**) 10,000 h, (**h**) 15,000 h.

Figure 12a shows the potentiodynamic polarization curve of Z3CN20-09M cast stainless steel in a 3.5% NaCl solution after different amounts of aging, of which the upper half is the anodic polarization curve and the lower half is the cathodic polarization curve. The corrosion current ($i_{corr.}$) can be calculated by the fixing the cross point of anode and cathode Tafel lines. The longitudinal coordinate is corrosion voltage. The corrosion current values

are shown in Table 2. Generally speaking, the corrosion rate (C_R) can be calculated from the following formula [32,33]: $C_R = \frac{i_{corr.} \cdot A_w}{zF\rho}$, where A_w is the molecular weight; z refers to the number of oxidation or valence states; F denotes the Faraday constant, which is 96,500 A·s/mol; and ρ is the density of the steel. The changes of corrosion potential and corrosion rate with thermal aging time are shown in Figure 12b. The corrosion potential of Z3CN20-09M stainless steel followed the trend: 0 h ≈ 1000 h > 10,000 h ≈ 3000 h > 272 h > 15,000 h > 6000 h. The largest corrosion potential variation between different samples was limited to ~0.1 V. The surface morphologies of the alloys after the corrosion tests are shown in Figure 13. The corrosion failure always occurred at the ferrite phase, and then the corrosion zones gradually increased. The corrosion rate increased significantly, which is in good agreement with the XPS analysis results.

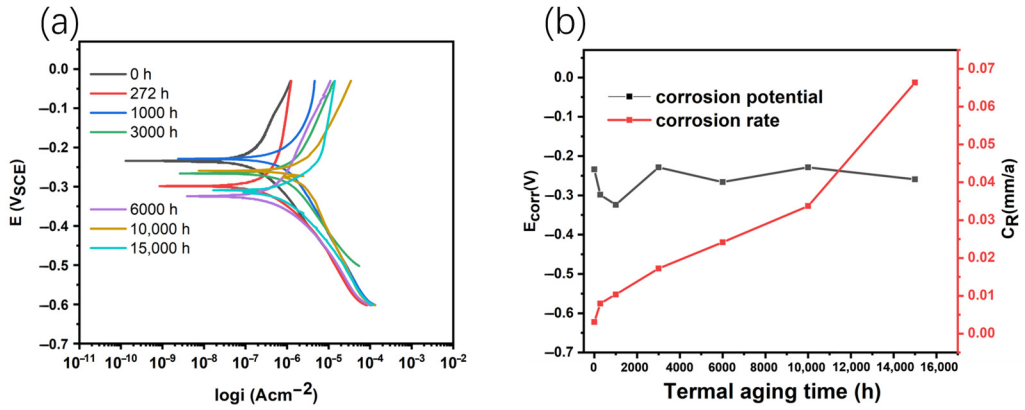

Figure 12. Potentiodynamic polarization curves (**a**), and the corrosion potential and corrosion rate (**b**) of Z3CN20-09M stainless steel at different aging times.

Table 2. The corrosion current of Z3CN20.09M cast stainless steel after thermal aging.

Thermal Aging Time(h)	0	272	1000	3000	6000	10,000	15,000
Corrosion current(A/cm^2)	2.4941×10^{-7}	6.4936×10^{-7}	8.4454×10^{-7}	1.4058×10^{-6}	1.9713×10^{-6}	2.7516×10^{-6}	5.4181×10^{-6}

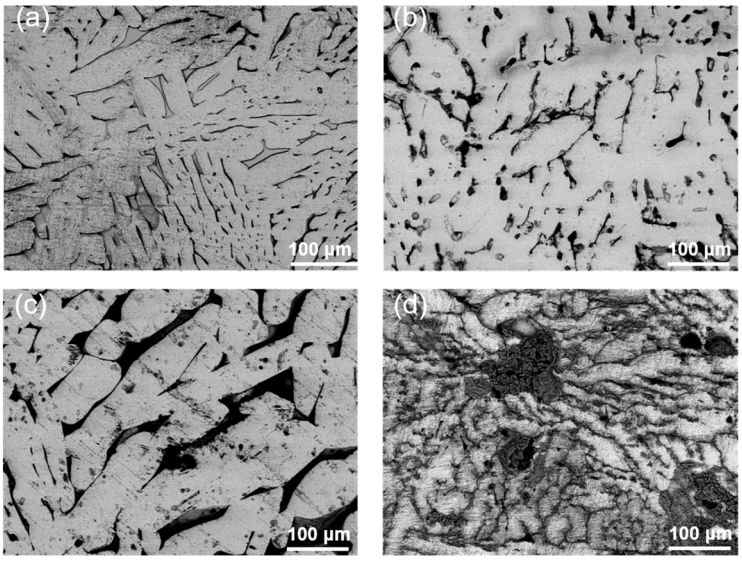

Figure 13. SEM images of corroded surface of Z3CN20-09M stainless steel under different thermal aging time (**a**) 0 h, (**b**) 1000 h, (**c**) 3000 h, (**d**) 15,000 h.

Chen et al. [34] studied the effect of thermal aging at 400 °C on the pitting behavior of Z3CN20.09M duplex stainless steel. It was found that during the amplitude-modulation decomposition process, a chromium-depleted region was formed around the α′ phase. At the interface, the micro-galvanic cell may be formed, thereby preferentially producing localized corrosion along the ferrite. It is believed that the Cr-rich α′phase is the main reason for the decrease in pitting corrosion performance of Z3CN20.09M steel after thermal aging. However, in this study, the corrosion rate continued to increase significantly during the formation of the G phase in the second stage of thermal aging. Due to the deficiency of Cr in G phases and concentration of Cr in matrix, severer corrosion occurred after more thermal aging. Therefore, the precipitation of the G phase may also be an important reason for the decline in corrosion performance.

4. Conclusions

During the 400 °C thermal aging treatment of Z3CN20-09M cast stainless steel, the morphology and content of ferrite and austenite do not change significantly. This proves that the changes in mechanical and corrosion properties after thermal aging are independent of the morphology of ferrite in steel. By applying HRTEM analysis, it was found that the G phase is only several or tens of nanometers in size, the content and size of which increase gradually during the course of thermal aging. The crystal structure and lattice constants of the G phase were determined by selected area electron diffraction, and the relationship between G phase and ferrite is cube-on-cube type. The impact toughness and microhardness change rapidly during the first 3000 h of thermal aging treatment; i.e., the changes in mechanical properties after thermal aging are mainly caused by the iron-rich phase (α) and the chromium-rich phase (α′) produced by ferrite amplitude-modulation decomposition. The corrosion resistance becomes increasingly worse during thermal aging, especially after 3000 h, which proves that the precipitation of G phase has a great influence on the corrosion resistance of Z3CN20-09M cast stainless steel.

Supplementary Materials: The following are available online at https://www.mdpi.com/article/10.3390/coatings11080870/s1. Figure S1: XPS energy spectrum of the iron of Z3CN20-09M stainless steel after different amounts of aging: (**a**) 0 h, (**b**) 272 h, (**c**) 544 h, (**d**) 1000 h, (**e**) 3000 h, (**f**) 6000 h, (**g**)10,000 h, (**h**) 15,000 h. Figure S2: XPS energy spectrum of the manganese of Z3CN20-09M stainless steel after different amounts of aging: (**a**) 0 h, (**b**) 272 h, (**c**) 544 h, (**d**) 1000 h, (**e**) 3000 h, (**f**) 6000 h, (**g**) 10,000 h, (**h**) 15,000 h.

Author Contributions: Conceptualization, F.X., F.S. and Y.L.; methodology, C.Z. and Q.Z.; formal analysis, F.X. and F.S.; investigation, F.X., C.Z. and Q.Z.; data curation, D.Y. and X.L.; writing—original draft preparation, F.X. and C.Z.; supervision, F.X. and Y.L. All authors have read and agreed to the published version of the manuscript.

Funding: This work was funded by the National Key Research and Development Program of China (2020YFB1901500), the Key-Area Research and Development Program of GuangDong Province (2019B010942001), the Natural Science Basic Research Program of Shaanxi (2021JM-011, 2020JM-516), the Open Fund of National Joint Engineering Research Center for abrasion control and molding of metal materials (HKDNM201901) and the Fundamental Research Funds for the Central Universities of China (xzy012019001, xtr0118008).

Institutional Review Board Statement: Not applicable.

Informed Consent Statement: Not applicable.

Data Availability Statement: Data sharing not applicable.

Acknowledgments: We thank Chang Huang, Renzijun, Jiao Li, Jiamei Liu and Chenyu Liang at the Instrument Analysis Center of Xi'an Jiaotong University for their assistance with XRD, SEM and TEM analysis.

Conflicts of Interest: The authors declare no conflict of interest.

References

1. Chopra, O.K.; Chung, H.M. Aging of cast duplex stainless steels in lwr systems. *Nucl. Eng. Des.* **1985**, *89*, 305–318. [CrossRef]
2. Liu, T.; Wang, W.; Qiang, W.; Shu, G. Mechanical properties and kinetics of thermally aged z3cn20.09m cast duplex stainless steel. *Int. J. Miner.* **2018**, *25*, 1148–1155. [CrossRef]
3. Park, C.; Kwon, H. Effects of aging at 475 °C on corrosion properties of tungsten-containing duplex stainless steels. *Corros. Sci.* **2002**, *44*, 2817–2830. [CrossRef]
4. Sahlaoui, H.; Makhlouf, K.; Sidhom, H.; Philibert, J. Effects of ageing conditions on the precipitates evolution, chromium depletion and intergranular corrosion susceptibility of aisi 316l: Experimental and modeling results. *Mater. Sci. Eng. A* **2004**, *372*, 98–108. [CrossRef]
5. Murty, K.L.; Ramaswamy, K. 1-Overview of Ageing and Degradation Issues in Light Water Reactors (LWRs). In *Materials Ageing and Degradation in Light Water Reactors*; Murty, K.L., Ed.; Woodhead Publishing Series in Energy: Cambridge, UK, 2013; pp. 3–69.
6. Lach, T.G.; Frazier, W.E.; Wang, J.; Devaraj, A.B.; Thak, S. Precipitation-site competition in duplex stainless steels: Cu clusters vs. spinodal decomposition interfaces as nucleation sites during thermal aging. *Acta Mater.* **2020**, *196*, 456–469. [CrossRef]
7. Guo, E.; Wang, M.; Jing, T.; Chawla, N. Temperature-dependent mechanical properties of an austenitic–ferritic stainless steel studied by in situ tensile loading in a scanning electron microscope (SEM). *Mater. Sci. Eng. A* **2013**, *580*, 159–168. [CrossRef]
8. Yamada, T.; Okano, S.; Kuwano, H. Mechanical property and microstructural change by thermal aging of SCS14A cast duplex stainless steel. *J. Nucl. Mater.* **2006**, *350*, 47–55. [CrossRef]
9. Tucker, J.D.; Miller, M.K.; Young, G.A. Assessment of thermal embrittlement in duplex stainless steels 2003 and 2205 for nuclear power applications. *Acta Mater.* **2015**, *87*, 15–24. [CrossRef]
10. Li, S.; Wang, Y.; Zhang, H.; Li, S.; Zheng, K.; Xue, F.; Wang, X. Microstructure evolution and impact fracture behaviors of Z3CN20-09M stainless steels after long-term thermal aging. *J. Nucl. Mater.* **2013**, *433*, 41–49. [CrossRef]
11. Xue, F.; Wang, Z.; Xue, F.; Wang, Z.; Shu, G.; Yu, W.; Shi, H.; Ti, W. Thermal aging effect on Z3CN20.09M cast duplex stainless steel. *Nucl. Eng. Des.* **2009**, *239*, 2217–2223. [CrossRef]
12. Yu, W.; Liu, Z.; Fan, M.; Gao, H.; Liu, E.; Chen, M.; Xue, F.; Chen, X. The effect of constraint on fracture properties of Z3CN20.09M after accelerated thermal aging. *Int. J. Press. Vessel. Pip.* **2021**, *190*, 104294. [CrossRef]
13. Fan, Y.; Liu, T.; Xin, L.; Han, Y.; Lu, Y.; Shoji, T. Thermal aging behaviors of duplex stainless steels used in nuclear power plant: A review. *J. Nucl. Mater.* **2020**, *544*, 152693. [CrossRef]
14. Viherkoski, M.; Huttunen-Saarivirta, E.; Isotahdon, E.; Uusitalo, M.; Tiainen, T.; Kuokkala, V.T. The effect of aging on heat-resistant cast stainless steels. *Mater. Sci. Eng. A* **2014**, *589*, 189–198. [CrossRef]
15. Hamaoka, T.; Nomoto, A.; Nishida, K.; Dohi, K.; Soneda, N. Accurate determination of the number density of g-phase precipitates in thermally aged duplex stainless steel. *Philos. Mag.* **2012**, *92*, 2716–2732. [CrossRef]
16. Erneman, J.; Schwind, M.; Andrén, H.O.; Nilsson, J.O.; Wilson, A.; Ågren, J. The evolution of primary and secondary niobium carbonitrides in AISI 347 stainless steel during manufacturing and long-term ageing. *Acta Mater.* **2006**, *54*, 67–76. [CrossRef]
17. Du, D.; Chen, K.; Yu, L.; Lu, H.; Zhang, L.; Shi, X.; Xu, X. SCC crack growth rate of cold worked 316l stainless steel in PWR environment. *J. Nucl. Mater.* **2015**, *456*, 228–234. [CrossRef]
18. Gutiérrez-Vargas, G.; Ruiz, A.; Kim, J.-Y.; López-Morelos, V.H.; Ambriz, R.R. Evaluation of thermal embrittlement in 2507 super duplex stainless steel using thermoelectric power. *Nucl. Eng. Technol.* **2019**, *51*, 1816–1821. [CrossRef]
19. Xie, X.; Ning, D.; Chen, B.; Lu, S.; Sun, J. Stress corrosion cracking behavior of cold-drawn 316 austenitic stainless steels in simulated PWR environment. *Corros. Sci.* **2016**, *112*, 576–584. [CrossRef]
20. Chopra, O.K.; Sather, A. *Initial Assessment of the Mechanisms and Significance of Low-Temperature Embrittlement of Cast Stainless Steels in LWR Systems*; United States Nuclear Regulatory Commission: Rockville, MD, USA, 1990; pp. 6–8.
21. Chung, H.M.; Leax, T.R. Embrittlement of laboratory and reactor aged CF3, CF8, and CF8M duplex stainless steels. *Mater. Sci. Technol.* **1990**, *6*, 249–262. [CrossRef]
22. Nakajima, Y.; Uno, Y.; Suzuki, M. Fracture toughness behaviour of service-exposed type 321 stainless steel at room and elevated temperature under normal and low straining rates. *Eng. Fract. Mech.* **1989**, *33*, 295–307. [CrossRef]
23. Coste, J.F.; Leborgne, J.M.; Massoud, J.P.; Borrelly, R. Development of A Portable Device for Thermoelectrical Power Measurement—Application to the Inspection of Duplex Stainless Steel Components. In *Review of Progress in Quantitative Nondestructive Evaluation*; Thompson, D.O., Chimenti, D.E., Eds.; Springer US: Boston, MA, USA, 1999; Volume 18, pp. 2095–2102.
24. Perez, M.; Massardier, V.; Kleber, X. Thermoelectric power applied to metallurgy: Principle and recent applications. *Int. J. Mater. Res.* **2009**, *100*, 1461–1466. [CrossRef]
25. Saillet, S.; Le Delliou, P. Prediction of J-R curves and thermoelectric power evolution of cast austenitic stainless steels after very long-term aging (200,000 h) at temperatures below 350 °C. *J. Nucl. Mater.* **2020**, *540*, 152328. [CrossRef]
26. Chandra, K.; Kain, V.; Raja, V.S.; Tewari, R.; Dey, G.K. Low Temperature thermal ageing embrittlement of austenitic stainless steel welds and its electrochemical assessment. *Corros. Sci.* **2012**, *54*, 278–290. [CrossRef]
27. Shiao, J.J.; Tsai, C.H.; Kai, J.J.; Huang, J.H. Aging embrittlement and lattice image analysis in a Fe-Cr-Ni duplex stainless steel aged at 400 °C. *J. Nucl. Mater.* **1994**, *217*, 269–278. [CrossRef]
28. Yang, M.; King Daniel, J.M.; Postugar, I.; Wen, Y.; Luan, J.; Kuhn, B.; Jiao, Z.; Wang, C.; Wenman, M.R.; Liu, X. Precipitation behavior in G-phase strengthened ferritic stainless steels. *Acta Mater.* **2021**, *205*, 116542. [CrossRef]

29. Li, S.; Wang, Y.; Wang, X.; Xue, F. G-Phase precipitation in duplex stainless steels after long-term thermal aging: A high-resolution transmission electron microscopy study. *J. Nucl. Mater.* **2014**, *452*, 382–388. [CrossRef]
30. Baylac, G.; Grandemange, J.M. The French code RCC-M: Design and construction rules for the mechanical components of PWR nuclear islands. *Nucl. Eng. Des.* **1991**, *129*, 239–254. [CrossRef]
31. Takeuchi, T.; Kameda, J.; Nagai, Y.; Toyama, T.; Nishiyama, Y.; Onizawa, K. Study on microstructural changes in thermally-aged stainless steel weld-overlay cladding of nuclear reactor pressure vessels by atom probe tomography. *J. Nucl. Mater.* **2011**, *415*, 198–204. [CrossRef]
32. Flitt, H.J.; Schweinsberg, D.P. A guide to polarisation curve interpretation: Deconstruction of experimental curves typical of the $Fe/H_2O/H^+/O_2$ corrosion system. *Corros. Sci.* **2005**, *47*, 2125–2156. [CrossRef]
33. Drażić, D.M.; Vascic, V. The Inflection point on the polarization curve and its use in corrosion rate measurements. *Corros. Sci.* **1985**, *25*, 483–491. [CrossRef]
34. Chen, Y.; Chen, B.; Dong, F.; Yang, B.; Li, S.; Yu, X. Pitting behavior of thermally aged Z3CN20.09M cast stainless steel for primary coolant pipe of nuclear power plant. *Eng. Fail. Anal.* **2018**, *83*, 1–8. [CrossRef]